Monitoring Subsurface Fracture Flow Using Unsupervised Deep Learning of Borehole Microseismic Waveform Data

Chenglong Duan, Lianjie Huang, Michael Gross, Michael Fehler, David Lumley, and Stanislav Glubokovskikh

***Abstract*— Fracture flow is the fluid movement in a fracture or a fracture zone. Since fracture flow can induce long-duration (LD) microseismic events, classifying different types of microseismicity is crucial for reliable monitoring of subsurface fracture flow. We analyze hydraulic fracturing-induced microseismic data recorded by borehole geophones and find four types of microseismic events: two types of short-duration events and two types of LD events. Among the two types of LD events, one contains frequency-drop LD (FDLD) characteristics, and the other exhibits low-frequency LD (LFLD) characteristics. We employ an unsupervised machine-learning algorithm based on the U-Net convolutional network to classify microseismic events. Our study shows that LFLD events occur only during the proppant injection period of hydraulic fracturing and that the spatiotemporal distributions of the LFLD events gradually grow from the fracture stimulation wells outward with time. Also, the cumulative seismic moment of the LFLD events is proportional to the cumulative amount of injected proppant. These results can be used to optimize hydraulic fracturing parameters in unconventional reservoirs.**

***Index Terms*— Deep learning, low-frequency long-duration (LFLD) event, microseismicity classification, time–frequency analysis.**

I. Introduction

LONG-DURATION (LD) events, characterized by their extended seismic duration, play an important role in understanding subsurface fluid flow dynamics and optimizing hydraulic stimulations [1], [2]. The time–frequency characteristics of LD events can be found in (deep-)volcanic tremors observed in Kilauea, Hawaii (1.5–3 Hz, several minutes) [3] and Mount St. Helens (∼1–2 Hz, 20 s) [4], [5], and those of tectonic tremors observed in Cascadia Subduction Zone (1–5 Hz, a few minutes to several days) [6], [7]. In exploration seismology, Das and Zoback [8] argue that the LD microseismicity lasts for tens of seconds and spans a frequency range of tens to hundreds of hertz, with moment magnitudes between −2 and −1. These studies showed that the source of LD events is likely to originate from subsurface fluid movement such as magma flows beneath volcanoes [9], [10], or injection-induced aseismic slip along fractures/faults [11], [12], [13] and tensile opening of a crack [14], [15]. Based on the relationship between subsurface fluid migration and LD events, we aim to classify the LD events from borehole microseismic waveform data during hydraulic fracturing and develop a fracture flow monitoring method using the most related types of LD events.

Locations and source mechanisms of microseismic events play key roles in the monitoring of hydraulic fracture propagation [16], [17], [18]. The techniques of physically inverting source parameters depend on an accurate subsurface velocity model that is often not available. They also require significant effort to evaluate the data quality and assess the accuracy and uncertainty of the inversion results. Furthermore, the data size of continuous seismic waveforms is usually in the order of terabytes. Therefore, it is impractical to manually examine and analyze such data that is often required for optimizing energy production and mitigating seismic hazards [19]. The emergence of machine-learning methods presents an opportunity for efficient data analyses. In seismology, machine learning has been used for source discrimination [20], event detection and phase picking [21], [22], [23], [24], [25], [26], phase association [27], [28], seismic wave simulation [29], and seismic signal labeling and classification [30], [31], [32]. For data clustering, Jenkins et al. [30] developed a machine-learning technique for low-frequency icequakes and earthquake data. Chien et al. [33] applied unsupervised clustering for microseismicity induced by fluid injection. Recently, Mousavi and Beroza [34] gave a thorough review of machine-learning methods in earthquake seismology.

For monitoring of subsurface fracture flow, we use a seven-layer U-Net convolutional neural network based on spectrograms to efficiently cluster high-frequency (up to ∼2 kHz) borehole seismic waveform data acquired during hydraulic stimulation. The output of the U-Net for a win-

Manuscript received 14 June 2023; revised 21 August 2023, 13 November 2023, and 7 February 2024; accepted 13 February 2024. Date of publication 23 February 2024; date of current version 6 March 2024. This work was supported in part by the U.S. Department of Energy (DOE) through the Los Alamos National Laboratory (LANL), which is operated by Triad National Security, LLC, for the National Nuclear Security Administration (NNSA) of U.S. DOE, under Contract 89233218CNA000001; and in part by the U.S. DOE, Office of Fossil Energy (work at the Lawrence Berkeley National Laboratory), under Contract DE-AC02-05CH1123. *(Corresponding authors: Chenglong Duan; Lianjie Huang.)*

Chenglong Duan was with Los Alamos National Laboratory, MS D452, Los Alamos, NM 87545 USA. He is now with the Department of Earth and Planetary Sciences, University of New Mexico, Albuquerque, NM 87131 USA (e-mail: chenglongduan.nju@gmail.com).

Lianjie Huang and Michael Gross are with Los Alamos National Laboratory, MS D452, Los Alamos, NM 87545 USA (e-mail: ljh@lanl.gov; michael_gross@lanl.gov).

Michael Fehler is with the Department of Earth, Atmospheric, and Planetary Sciences, Massachusetts Institute of Technology, Cambridge, MA 02139 USA (e-mail: fehler@mit.edu).

David Lumley is with the Department of Sustainable Earth Systems Sciences and Department of Physics, University of Texas at Dallas, Richardson, TX 75080 USA (e-mail: david.lumley@utdallas.edu).

Stanislav Glubokovskikh is with Lawrence Berkeley National Laboratory, Berkeley, CA 94720 USA (e-mail: sglubokovskikh@lbl.gov).

Digital Object Identifier 10.1109/TGRS.2024.3369577

© 2024 The Authors. This work is licensed under a Creative Commons Attribution-NonCommercial-NoDerivatives 4.0 License.
For more information, see https://creativecommons.org/licenses/by-nc-nd/4.0/

dowed seismic waveform dataset is a lower-dimensional latent vector containing image features. We use these latent feature vectors to perform Gaussian mixture model (GMM) clustering. Our analysis shows that there exist four different types of microseismic events: two distinct types of LD events and two types of short-duration events. One type of LD event has the characteristics of frequency-drop long-duration (FDLD), and the other type of LD event contains the characteristics of low-frequency long-duration (LFLD). We explore the correlations between LFLD events and proppant injection histories, cumulative seismic moments, and spatiotemporal evolution of event locations. Our results demonstrate that only one type of LD event, the LFLD event, can be used to monitor fracture flow.

II. Dataset

Our study area is located at the Permian Basin Wolfcamp shale formation in the Midland Basin, Reagan County, Texas [see Fig. 1(a)]. This unconventional oil and gas production site contains 11 horizontal injection wells and 37–49 hydraulic stimulation stages in total [see Fig. 1(b)]. We analyze microseismic data recorded during Stage 25 in treatment well 1 and Stage 25 in treatment well 2, which we refer to as HF-1 and HF-2 for brevity.

The monitoring wells shown in Fig. 1(b) include a horizontal well (with MH-1 and MH-2 arrays) and a vertical well (with MV-1 array), and borehole geophones installed in these wells continuously recorded microseismic data during hydraulic fracturing stimulation in the two treatment wells with a sampling rate of 4 kHz. The geophone arrays of MH-1 and MV-1 were used to record microseismic data during Stage HF-1, while those of MH-2 and MV-1 were used to acquire microseismic data during Stage HF-2. In each case, the seismic waveforms contain 54 traces from 18 three-component borehole geophones with a resonant frequency of 15 Hz.

We use the following procedure to process the seismic data: 1) extract the continuous seismic data for the time intervals corresponding to the injection times in the two stages (see the time axes in Fig. 2); 2) remove the instrument response from the waveforms; and 3) bandpass filter the data to 10–1900 Hz to suppress low and high-frequency noise in the data. The processed common-receiver (geophone ST00) waveforms of Stages HF-1 and HF-2 are shown in Fig. 2 (top). We select 193 microseismic events from the microseismic event catalog provided by the project contractor [35] for Stage HF-1 and 646 events for Stage HF-2 [see Fig. 1(b)], which are spatially distributed around the corresponding fracturing stages. The catalog contains event origin times, locations, and moment magnitudes that are used in this study. HF-1 and HF-2 in Fig. 2 (bottom) show histograms of numbers of events within 30-s intervals during the stimulations. Given an average event magnitude of −2.2 and a source-receiver distance of less than 300 m, our data contain frequencies up to 2 kHz. This is due to the small source magnitudes and weak seismic wave attenuation within the short source-receiver distances. This high-frequency feature of the data is different from most other studies on LD events that are based on low-frequency data of tens of hertz.

Using the 839 events from the microseismic catalog, we obtain 10 325 samples over all 18 geophones for Stages HF-1 and HF-2 in total (here each sample for each event contains a seismogram, a spectrogram, and event metadata), and store them as the HDF5 data format for the event classification procedure.

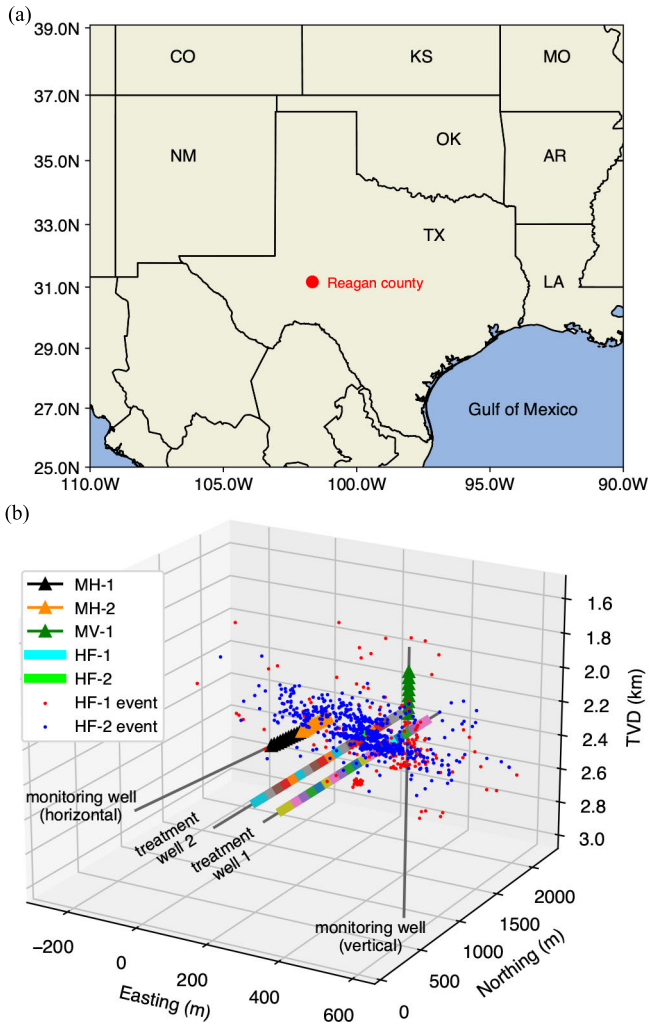

Fig. 1. Fluid injection stimulation and microseismicity monitoring system. (a) Location of the Wolfcamp shale formation in the Midland basin, Reagan County, Texas. (b) Three-dimensional view of the fluid injection for hydraulic fracturing. Triangles denote three-component geophones, and rectangles denote multistage injection simulation sections. Red dots are locations of microseismic events accompanying Stage HF-1, and blue dots are those accompanying Stage HF-2. The depth axis "TVD" means true vertical depth, which is measured relative to a point at the ground surface.

III. Methods

A. Spectrogram Calculation of Microseismic Waveform Data

The short-time Fourier transform (STFT) to compute the time–frequency representation of a seismic trace is expressed as

$$S(\tau, \omega) = \left| \int_0^\infty s(t) w(t-\tau) e^{-i\omega t} dt \right| \tag{1}$$

where $S(\tau, \omega)$ denotes a spectrogram of a time-domain seismic waveform $s(t)$, τ is the time, ω is the angular frequency, $w(\tau)$ is a window function, and i denotes the imaginary unit. We compute STFT for all vertical-component waveforms of 18 borehole geophones. We use only one component of the

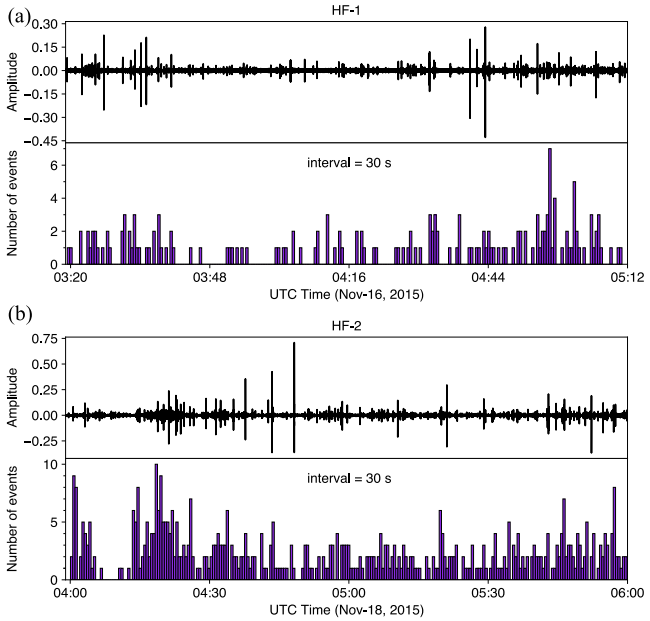

Fig. 2. Totally detected microseismicity. (a) and (b) (Top) Waveforms recorded at geophone ST00 for Stages HF-1 and HF-2, respectively. (a) and (b) (Bottom) Temporal distribution of 193 and 646 microseismic events, respectively, within consecutive 30 s time intervals.

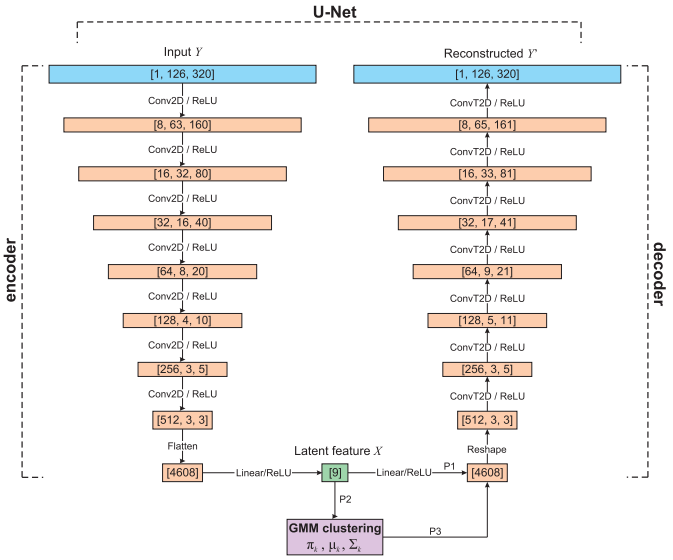

Fig. 3. Network architecture for encoder–decoder (U-Net) and GMM clustering for predicting the class of spectrograms. The numbers in the brackets denote the size of the tensor in each layer. The input spectrogram has a size of 126 × 320, where the first dimension is the frequency, and the second dimension is time. The notations between layers are as follows: "Conv2D" is a 2-D convolution operator; "Linear" is a linear transformation; "Flatten" reshapes to a 1-D tensor; "ConvT2D" is a 2-D transposed convolution operator; and "ReLU" is rectified linear unit function defined as $\mathrm{ReLU}(x) = \max(0, x)$.

seismogram to have less data to deal with. We apply the Kaiser window (a kind of taper using the Bessel function) [36] to (1) with a shape parameter of $\beta = 5.7$, a window length of 0.0625 s, an overlapping ratio between two segments of 0.98, and FFT window length of 250 points. We choose these STFT parameters to ensure a balanced resolution between frequency and time. We take a 0.8 s time window centered at the peak amplitude of a catalog event and make sure that only one event exists within this time window. A 0.8 s trace yields 320 time samples per spectrogram.

We consider the spectrograms of the waveforms as 2-D images sampled by pixels. Since the decibel scale magnifies small amplitudes (i.e., singularities) that appear as background noise in the spectrograms, we scale the original spectrograms using a fractional power given by

$$I(\tau, \omega) = S(\tau, \omega)^{1/p}, \quad (p > 1) \tag{2}$$

where $p = 2$. We use the scaled spectrogram image $I(\tau, \omega)$ to train our machine-learning algorithm. We employ (2) to enhance the lower energy of high-frequency parts in the spectrograms. Furthermore, we truncate the spectrograms using a 0.8 s time window centered at the peak amplitude among all frequencies and a cosine-taper at both ends.

B. U-Net Autoencoder Neural Network

High-dimensional input data, such as spectrograms, are difficult to cluster [37], [38]. A lower-dimensional representation of the input data makes it easier and more feasible to obtain a meaningful clustering result [30]. Here, we construct a U-Net architecture using a seven-layer 2-D convolutional (Conv2D) neural network for the encoder process and a transposed convolutional (ConvT2D) neural network for the decoder process (see Fig. 3). The numbers in the brackets represent [channel, height, width] of an image. For example, the input layer Y is composed of one channel, 126 frequency samples, and 320-time samples within a duration of 0.8 s, which corresponds to the dimensions of the spectrograms that need to be reconstructed (Y'). The encoder segment generates a "compressed" nine-element latent feature vector, namely, latent feature X. The first step (Route P1 in Fig. 3) is training the model weights iteratively. We implement the mean-squared-error (mse) function to measure the loss between Y and Y' (see Section III-C for details). The next step (Route P2 in Fig. 3) is performing GMM clustering (in other words, event label prediction) for the unlabeled latent feature X derived from the trained model (see Section III-D for details). The last step (Route P3 in Fig. 3) is using the labeled latent features and running the decoder segment to generate the classified waveforms, spectrograms, and event metadata for spatiotemporal correlation analysis.

C. Spectrogram-Based Training and Validation

Fig. 4 shows how we window the seismograms and the spectrograms for visualization throughout this article. Based on the events catalog, we first window a 0.25 s waveform starting from the event origin time and mark the 0.125 s as the middle point of the time window. Centered at the middle point, we extend both sides by 0.4 s to make a 0.8 s waveform as the input data for training. When plotting the spectrogram and its corresponding seismogram, we find the maximum spectrogram amplitude and then extend both sides away from the maximum amplitude point by 0.2 s.

In the encoder–decoder deep learning network, we employ a randomly chosen subset of 8261 samples for training purposes and 2064 samples for validation, among the total of 10 325

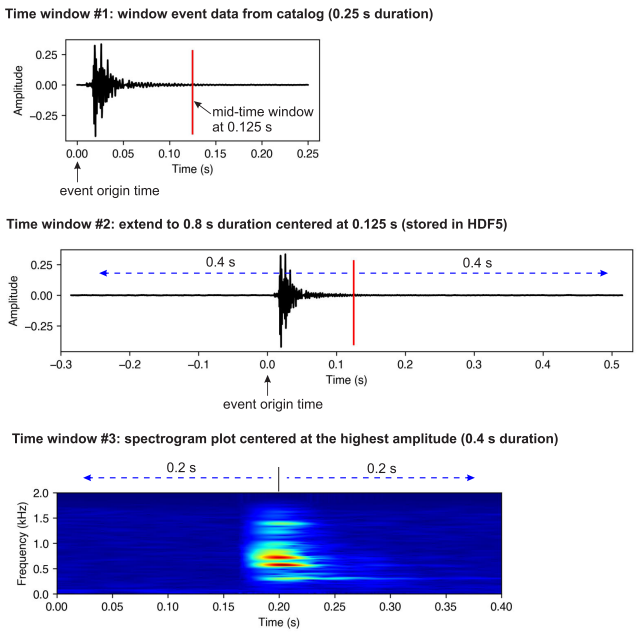

Fig. 4. Illustration of the time windows for input seismograms (time windows 1 and 2), and for spectrogram visualizations in this article (time window 3). The duration of the input seismogram is 0.8 s, while the duration for spectrogram visualization is 0.4 s.

samples. We use the following mse misfit function to quantify the loss in each iteration:

$$L(\mathbf{y}, \mathbf{y}') = \frac{1}{MN} \sum_{i=1}^{N} \sum_{j=1}^{M} \left(y_{ij} - y'_{ij}\right)^2 \tag{3}$$

where $\mathbf{y}$ and $\mathbf{y}'$ are the input and reconstructed spectrograms, respectively, N denotes the mini-batch size (a to-be-determined hyperparameter), and M represents the count of grid points within each input spectrogram (40 320 for this study). Here, the reconstructed spectrograms "reproduce" the most useful signal properties that resemble the input spectrograms via the U-Net training process [39]. We implement a rectified linear unit (ReLU) activation function between every pair of convolutional neural layers, the same for transposed convolutional layers (see Fig. 3). In each iteration, we employ the Adam optimization method [40] with the stochastic gradient descent to update the model weights.

We utilize a grid search method to determine the optimal hyper-parameters for the U-Net training, with an initial learning rate of $l_r = 0.0001$ and a mini-batch size of $N = 64$. Fig. 5(a) shows the learning curve for training, indicating that the recognition of patterns given the ground-truth spectrogram results in a less than 20% mse loss. The validation loss stays close to the training loss, and both curves converge at the 74th epoch. The plateau of the learning curve in Fig. 5(a) is likely due to nonlinear complexity and gradient-based optimization, which takes several iterations/epochs to move away from the plateau until the algorithm starts converging rapidly again. To test the training results for the entire microseismic dataset, we input all the spectrograms to the trained model, and the average mse loss is 6.0645×10^{-6}, which agrees with the validation loss in the convergence range. Fig. 5(b) illustrates the training results of the final iteration by selecting four different time–frequency event types. The

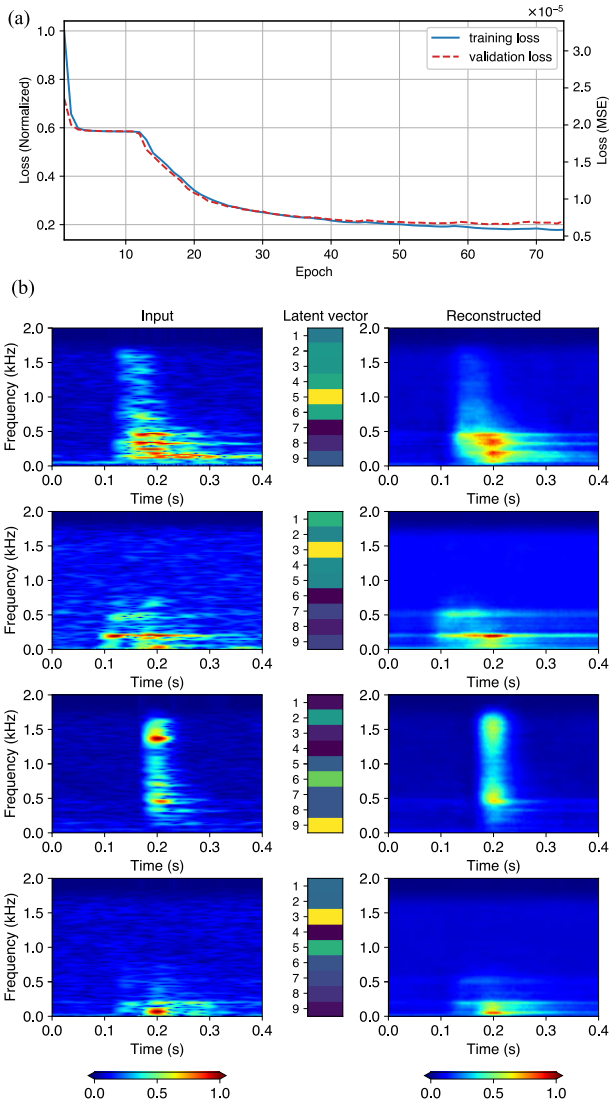

Fig. 5. Spectrogram training results. (a) Learning curves for training and validation. The left vertical axis is the normalized loss to represent percentage change based on the absolute mse loss of the right vertical axis. (b) Results of the final epoch using four different time–frequency types of events. (Left) Ground-truth spectrograms. The middle column shows the latent feature vectors after the encoder process. (Right) Reconstructed spectrograms using the latent features.

reconstructed spectrograms preserve the major frequency content and time-duration features, but are smoother than the input spectrograms, suggesting that the latent vector stores LD features and can be used to distinguish LFLD and FDLD events from the other short-duration event types. An alternative solution to this issue is to employ supervised deep-learning algorithms. With prior labeling knowledge, small details in the spectrograms can be well learned. For our project, we do not have enough datasets to perform labeling, which is one of the reasons for us to choose unsupervised deep learning methods.

D. Clustering Using GMM

The likelihood distribution for GMM is given by [41], [42]

$$p(\mathbf{x}_n) = \sum_{k=1}^{K} \pi_k \mathcal{N}(\mathbf{x}_n | \mu_k, \Sigma_k) \tag{4}$$

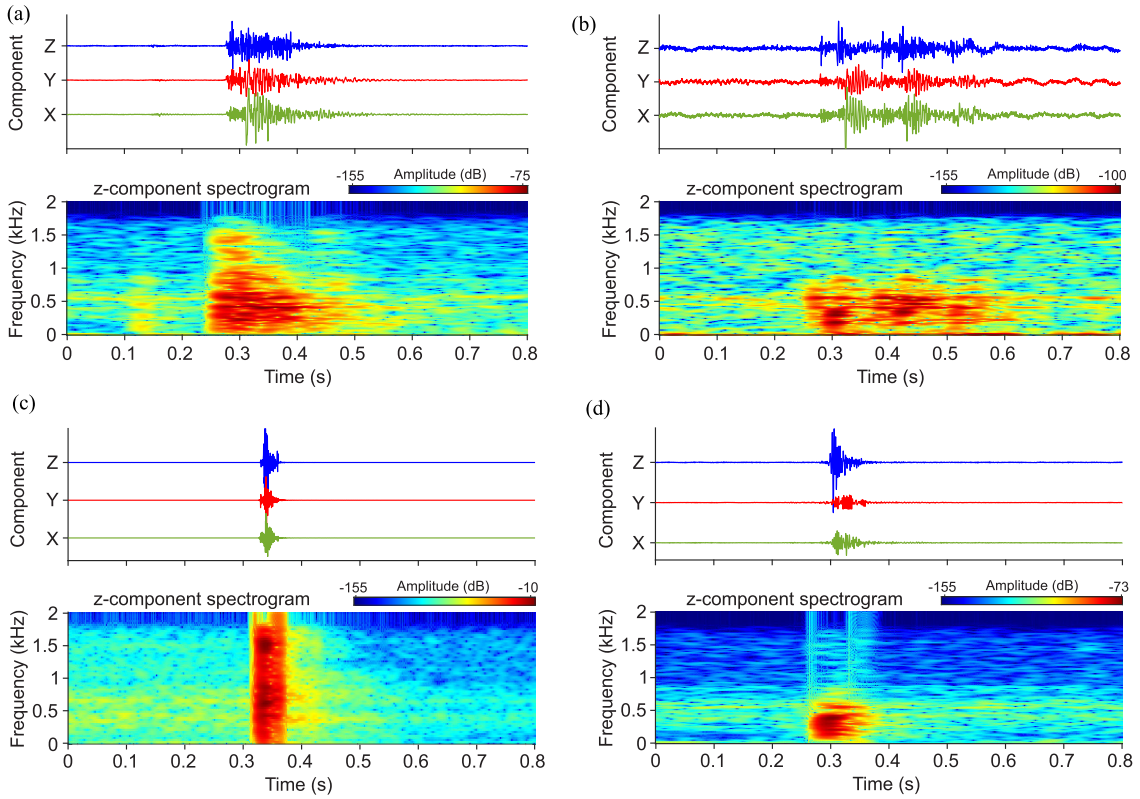

Fig. 6. Examples of four distinct types of microseismic events. (a) FDLD event. (b) LFLD event. (c) High-frequency short-duration event (HFSD). (d) Low-frequency short-duration event (LFSD). (Top) Three-component waveforms. (Bottom) z-component spectrograms in decibel scale.

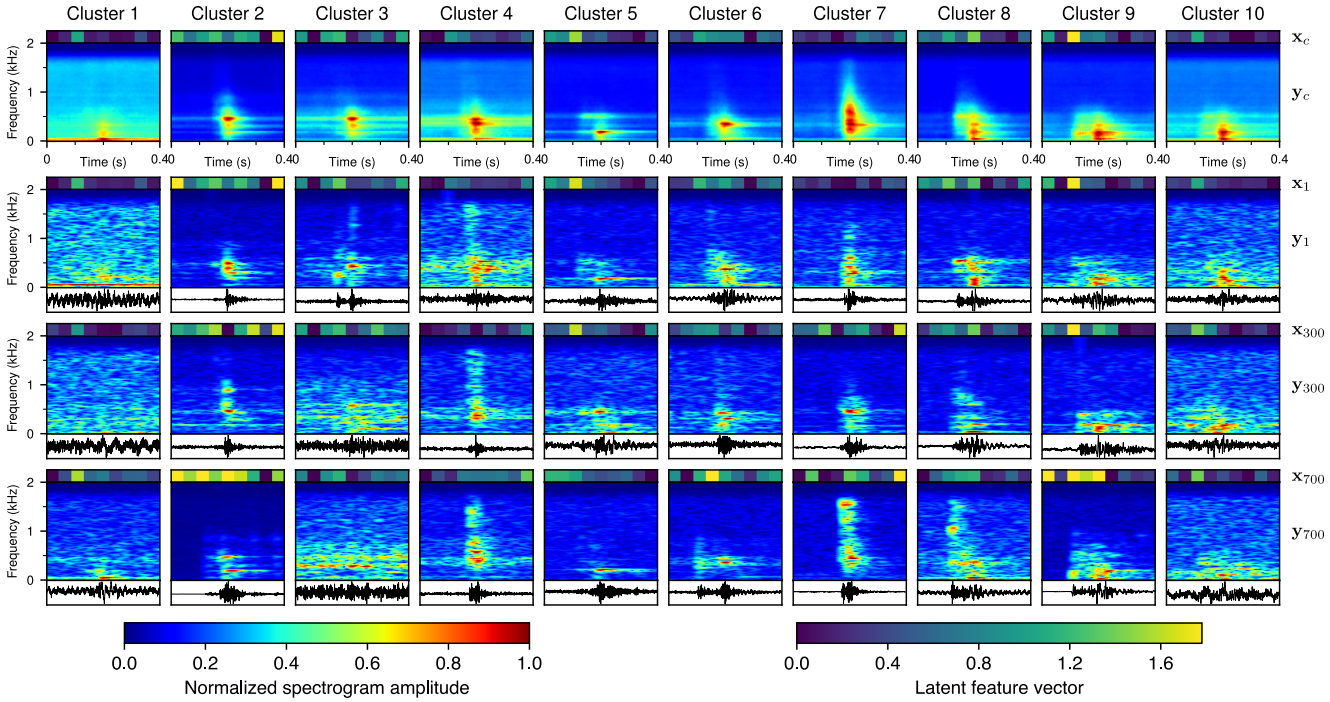

Fig. 7. GMM clustering results for microseismic events. Columns show the labeled spectrograms with the same cluster number from 1 to 10. The top row shows the maximum likelihood (centroid) predictions in respective clusters with latent features ($\mathbf{x}_c$) and reconstructed spectrograms ($\mathbf{y}_c$). Rows 2–4 illustrate samples with ascending distances from the centroid prediction of the cluster, denoted by the subscripts 1, 300, and 700. (Top to bottom) Each subplot is arranged with the nine-element latent feature vector ($\mathbf{x}_1$, $\mathbf{x}_{300}$, and $\mathbf{x}_{700}$), the ground-truth spectrogram ($\mathbf{y}_1$, $\mathbf{y}_{300}$, and $\mathbf{y}_{700}$), and the ground-truth seismogram. All subplots share the same horizontal axis (time in seconds) and vertical axis (frequency in kilohertz).

where $\mathbf{x}_n$ denotes the latent feature vector obtained from the encoder segment, K is the number of clusters, a to-be-determined hyperparameter, $\mathcal{N}$ represents the normal distribution, π_k is the mixing probability, μ_k is the mean value, and Σ_k is the covariance of kth cluster. Multiplying $p(\mathbf{x}_1)p(\mathbf{x}_2), \ldots, p(\mathbf{x}_N)$ and taking logarithm on both sides,

the logarithm of the joint probability for all latent features is given by

$$\ln p(\mathbf{x}) = \sum_{n=1}^{N} \ln p(\mathbf{x}_n) \tag{5}$$

where N is the total number of samples. To determine (π_k, μ_k, Σ_k) in (4), we employ the expectation-maximization algorithm [41] to iteratively update them using

$$\pi_k^* = \frac{\sum_{n=1}^{N} \gamma_{nk}}{N} \tag{6}$$

$$\mu_k^* = \frac{\sum_{n=1}^{N} \gamma_{nk}\mathbf{x}_n}{\sum_{n=1}^{N} \gamma_{nk}} \tag{7}$$

$$\Sigma_k^* = \frac{\sum_{n=1}^{N} \gamma_{nk}||\mathbf{x}_n - \mu_k||_2}{\sum_{n=1}^{N} \gamma_{nk}} \tag{8}$$

until the logarithmic probability (5) converges. The intermediate probability γ_{nk} in (6)–(8) can be calculated using

$$\gamma_{\text{nk}} = \frac{\pi_k \mathcal{N}(\mathbf{x}_n|\mu_k, \Sigma_k)}{\sum_{j=1}^{K} \pi_j \mathcal{N}(\mathbf{x}_n|\mu_j, \Sigma_j)}. \tag{9}$$

IV. Results

A. Two Types of LD Microseismic Events

By visually inspecting the data, we present four different types of microseismic events in Fig. 6. The top panel of each subfigure illustrates waveforms recorded by geophone ST00 located in the vertical monitoring well, while the bottom panel shows the spectrograms of the z-component waveforms.

We observe two types of LD events. The first type, FDLD exhibits approximately 1600 Hz at the event start time (0.25 s), and it decreases to 500 Hz at the event end time (0.5 s) [see Fig. 6(a)]. The second type of event is characterized by relatively low-frequency signals of up to approximately 500 Hz from the event start time at 0.25 s to the event end time at 0.6 s, namely, LFLD [see Fig. 6(b)]. These two types of LD events last hundreds of cycles. By contrast, the spectrograms in Fig. 6(c) and (d) indicate that these events last for less than 0.1 s, or about ten cycles. The event in Fig. 6(c) contains high-frequency signals of up to 1600 Hz, and that in Fig. 6(d) comprises only low-frequency signals of up to 500 Hz. We call these events short-duration events.

B. Event Categorization

We use spectrograms of borehole microseismic data and our deep learning clustering method to extract LD events. Fig. 7 shows a gallery of spectrogram clustering results. As an illustration, we show the maximum likelihood prediction and three ground-truth datasets for each category. By visually comparing the clustered events, this clustering result indicates that microseismic events are labeled not only by the time–frequency patterns, but also by the signal-to-noise ratios (SNRs). For instance, Cluster 1 contains the lowest SNR events; Clusters 2 and 3 are low-frequency short-duration events with higher SNR events in Cluster 2 and lower SNR events in Cluster 3; Clusters 4 and 7 comprise high-frequency short-duration events; and Cluster 6 events contain dominant high-frequency energy. Clusters 5, 9, and 10 are LFLD events, and Cluster 8 consists of FDLD events.

We perform deep learning and clustering of HF-1 and HF-2 microseismic data using only one GPU. As shown in Table I,

TABLE I

Computation Cost of Training and Clustering. The First Row Shows the GPU Parameters. The Size of the Dataset Used for Training and Validation Is 165 GB

GPU	Name	Number	Memory
	NVIDIA Quadro M2000	1	4239 MB
Runtime (hour:min:sec)	**Training and validation**		**Clustering**
	29:51:33.46		0:2:4.16

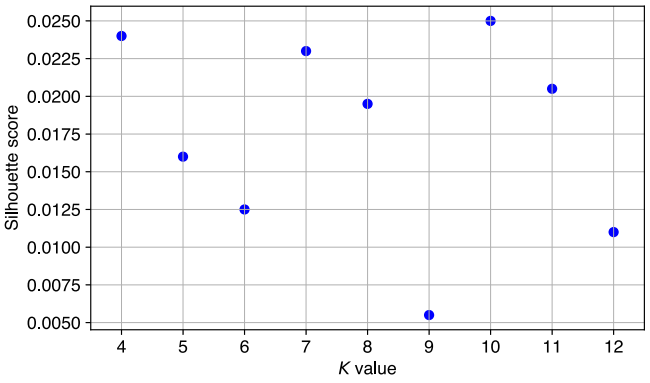

Fig. 8. Optimal Silhouette score search for $K = 4$–12.

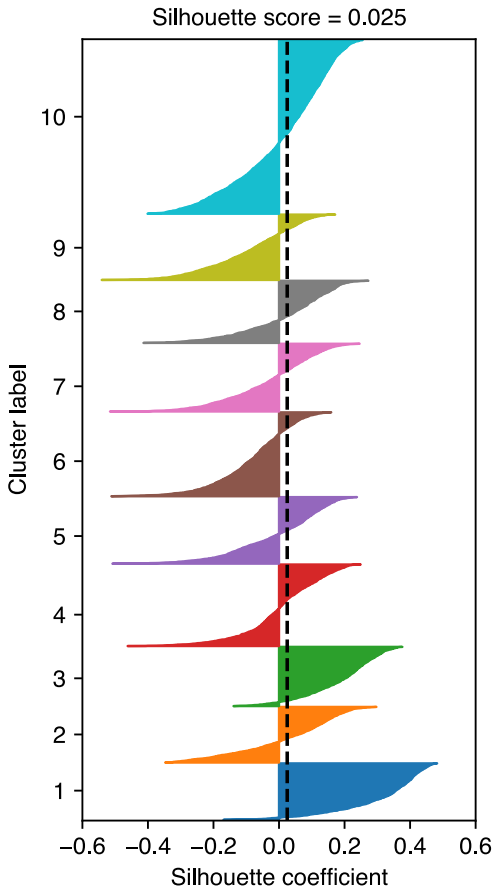

Fig. 9. Silhouette analysis for clustered events in $K = 10$. The dashed line represents the mean Silhouette score for all the clustered events.

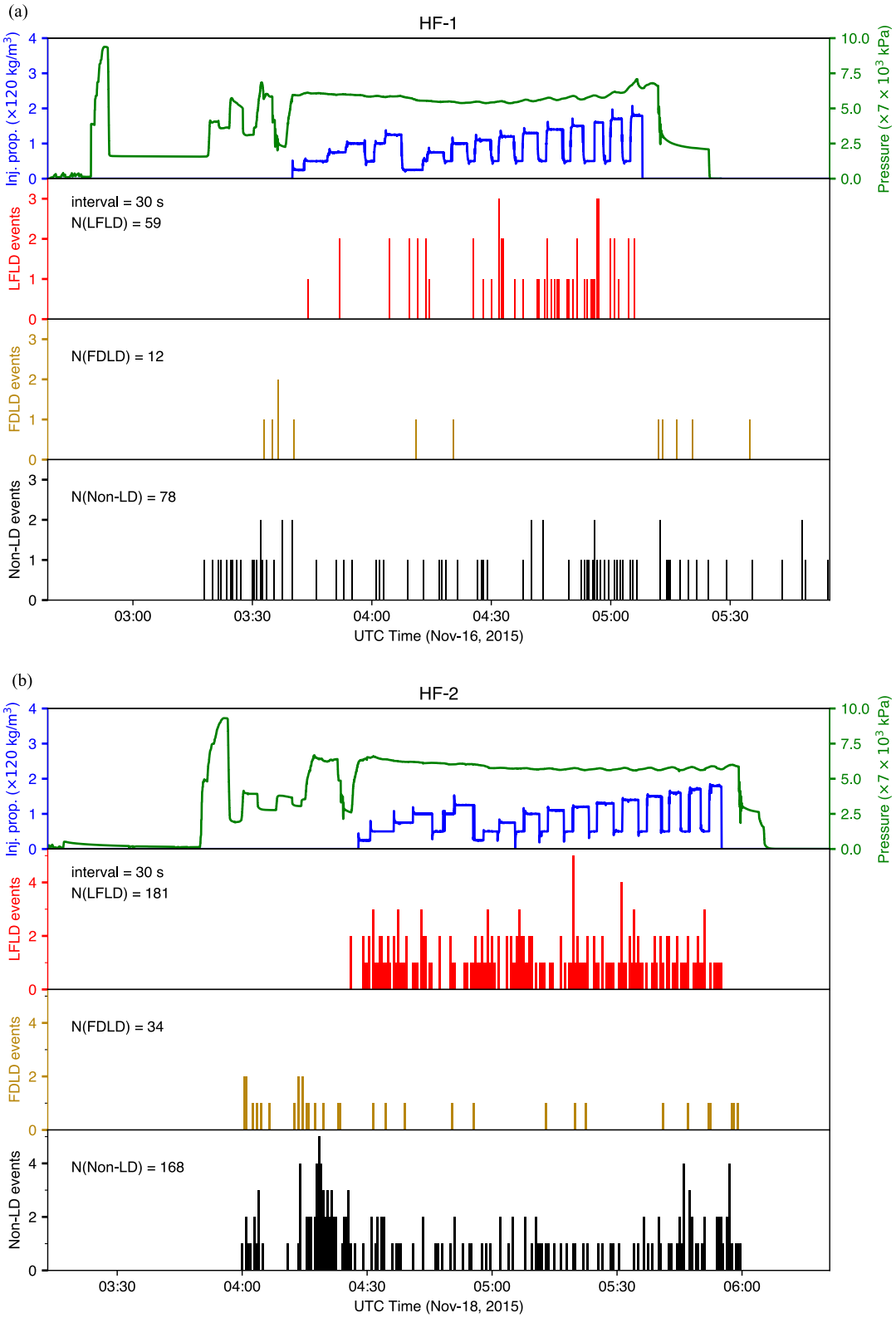

Fig. 10. Comparisons of the injected proppant density and pressure with the occurrence times of the LFLD, FDLD, and non-LD events. (a) Injection stage HF-1. (b) Injection stage HF-2. We use the history of the injected proppant density (i.e., "Inj. prop." shown in the top) to represent the occurrence of proppant injection. The number of events is counted with an interval of 30 s. "N(LFLD)," "N(FDLD)," and "N(Non-LD)" denote the classified numbers of LFLD events, FDLD events, and non-LD events, respectively.

although the training and validation time takes more than 1 day, the clustering of microseismic events takes only about 2 min for a specific categorization. The major computation cost is spent on the training and validation process.

To test the reliability of the clustered results, we perform Silhouette analysis [43] for the clustered microseismic events in the latent vector domain. The Silhouette scores among various K values from 4 to 12 with an increment of 1 are

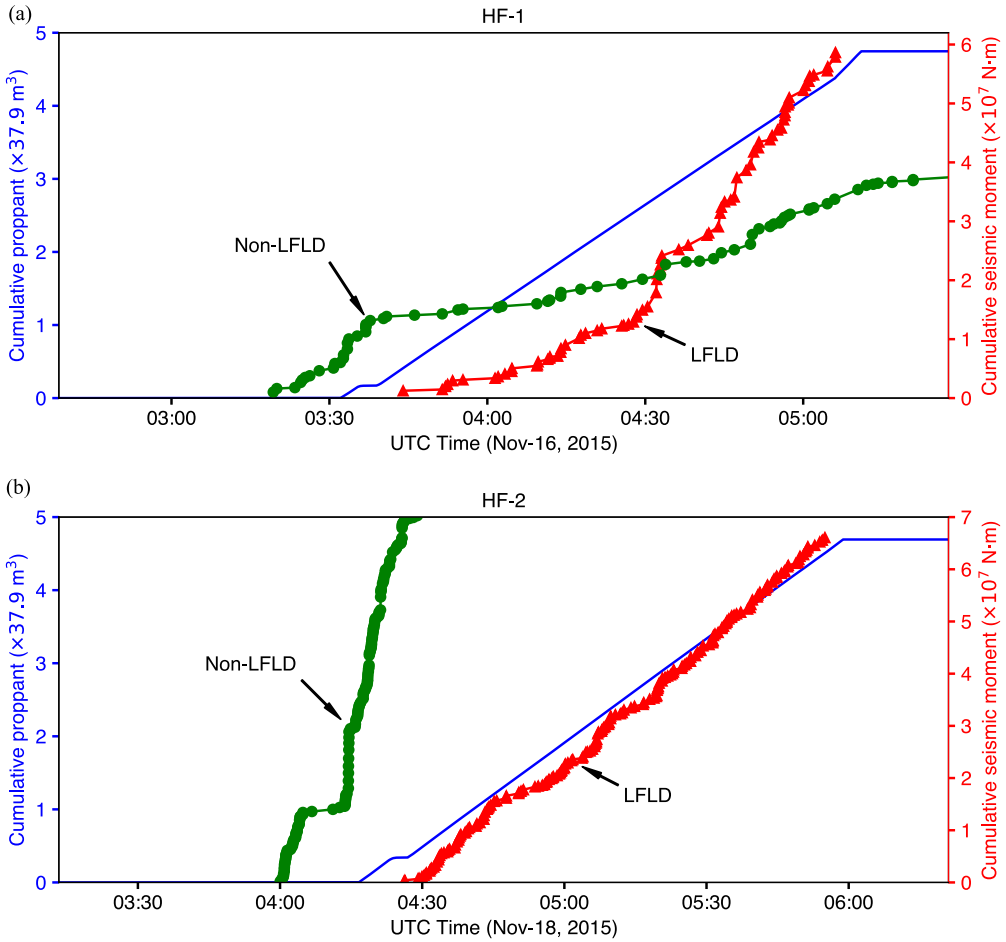

Fig. 11. Relationships between the cumulative proppant injection volume and the cumulative seismic moment of the LFLD and non-LFLD events. (a) Injection stage HF-1. (b) Injection stage HF-2.

shown in Fig. 8. The maximum Silhouette score is 0.025 when $K = 10$, which indicates that $K = 10$ is the optimal number of clusters. According to the Silhouette coefficients of each component in the optimal number of clusters $K = 10$ (see Fig. 9), clusters 6, 7, and 9 are not well separated because more events have negative Silhouette coefficients than positive Silhouette coefficients, while the other clusters have more events with positive Silhouette coefficients.

C. Injection Period and Event Occurrence Times

During hydraulic stimulation, fracture propagation is closely related to injected fluid volume, as shown by earthquake hypocenter analysis [44] and fracture mechanics modeling [45]. However, the spatiotemporal relationship between LD seismicity and fluid flow/fracture development has rarely been studied.

Fig. 10(a) and (b) (top) shows histories of pressure (green curves) and injected proppant density (blue curves) for Stages HF-1 and HF-2, respectively (proppant is a solid granular material – unconsolidated sand for example—used to keep a hydraulic fracture open). In practice, fracturing fluid (usually $\geq$ 98% water) is injected first into the reservoir stimulation region, which aims to increase pore pressure and create initial fractures. This process is demonstrated from 02:50–03:40 (hour: minute, same notation below) for Stage HF-1 and 03:50–04:25 for Stage HF-2 when the pressure curves fluctuate the most (see Fig. 10). Proppant is injected into HF-1 during 03:40–05:10 and into HF-2 during 04:25–05:55, and the pressure is almost constant during proppant injection, as shown in Fig. 10.

Fig. 10 also depicts histograms of clustered LFLD, FDLD, and nonlong-duration (non-LD) events as a function of time for Stages HF-1 [see Fig. 10(a)] and HF-2 [see Fig. 10(b)]. The sample interval for the histograms is 30 s. We find that the LFLD events occurred mainly during the proppant injection period, and the FDLD and non-LD evens were induced before, during, and after the proppant injection period. The FDLD event catalog may not be complete because FDLD events are more complex and thus more difficult to detect than LFLD and non-LD events. Because the LFLD events occurred during the proppant injection period as shown in Fig. 10 (top), we hypothesize the following mechanism of fluid flow in a fractured rock system. During the initial period of fluid injection, cracks are created, and the effective stress is reduced, inducing the early stage microseismicity. Without proppant, most cracks return to a closed state. The proppant injection dilates the created fractures and forms unhindered conduits for fluid flow [46]. The oscillation of fluid flow within these opened fractures results in new fractures, inducing the LFLD events.

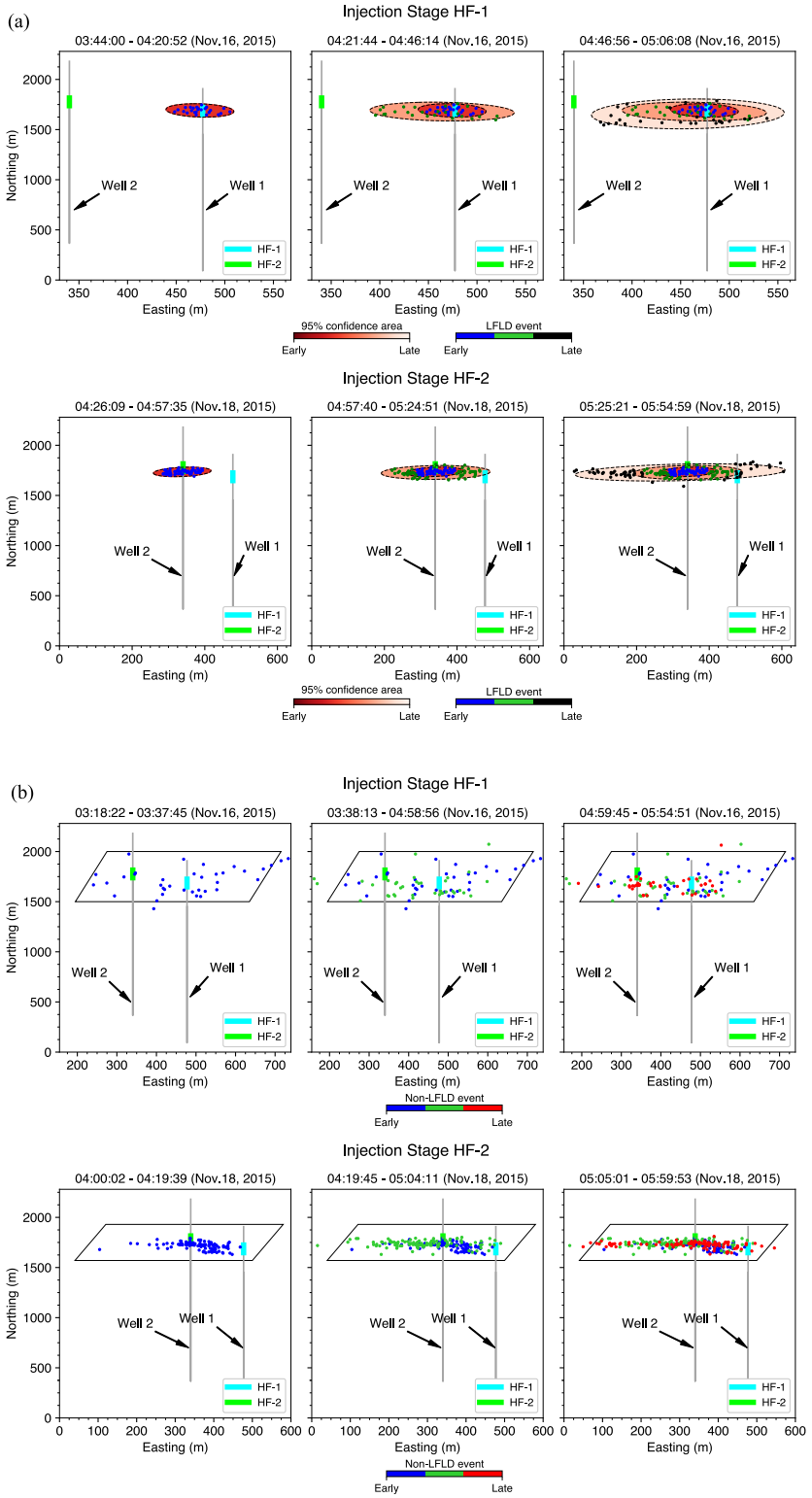

Fig. 12. Spatiotemporal distributions of LFLD and non-LFLD events projected onto an east-north plane parallel to the horizontal treatment wells 1 and 2. Three-time intervals (marked at the top of each panel) are used to show the evolutions of the LFLD and non-LFLD events during the two hydraulic fracturing stages. "Well 1" and "Well 2" represent the two horizontal treatment wells from which the fluid injection stages HF-1 and HF-2 are positioned, respectively. (a) Blue, green, and black dots are the LFLD event locations with respect to the above time intervals for injection stages HF-1 and HF-2, respectively. The 95% confidence ellipses have dark colors for relatively early time while light colors for relatively late time. (b) Blue, green, and red dots are the non-LFLD event locations with respect to the three-time intervals for injection stages HF-1 and HF-2, respectively.

D. Cumulative Seismic Moment of LFLD Events

We then investigate the relationship between the cumulative seismic moment of LFLD events and the cumulative proppant injection volume, as displayed in Fig. 11. The seismic moment (M_0) is determined using

$$M_0 = 10^{1.5M_w+9.1} \tag{10}$$

where M_w is the moment magnitude of microseismicity in Newton meters (N · m) [47]. The cumulative seismic moment

can approximate the released seismic energy of an earthquake sequence. The cumulative seismic moment of LFLD events exhibits a similar trend to the curves of the cumulative proppant injection volume. For Stage HF-1, the cumulative seismic moment of the LFLD events increases linearly as the cumulative proppant injection volume growths [see Fig. 11(a)]. For Stage HF-2, the cumulative seismic moment of the LFLD events shows a better linear relationship with the cumulative proppant injection volume [see Fig. 11(b)], partially because Stage HF-2 contains more detected LFLD events than Stage HF-1. In addition, using the same vertical axis for plotting LFLD events, the cumulative seismic moment of non-LFLD events does not correlate well with the cumulative proppant volume curves (see Fig. 11).

Bentz et al. [48] found a proportional relationship between the cumulative seismic moment and the cumulative volume of fluid injected. Our results further reveal that such a linear relationship is better reflected in LFLD events than in non-LFLD events. This relationship improves the estimate of the released seismic energy in hydraulic fracturing. It also provides practical insight into monitoring the progress of fracture creation, which may help optimize proppant injection parameters in future work.

E. Spatiotemporal Evolution of Microseismic Events

If our above hypothesis is correct, the detection of LFLD events provides a new means for monitoring the fluid and proppant flow through newly created fractures accompanying fluid injection. Spatiotemporal evolutions of LFLD events can further validate our hypothesis. We extract the LFLD event locations from the microseismic catalog provided by Stegent and Candler [35]. We divide the total time duration of the LFLD events into three equal time intervals with the starting time being the occurrence time of the first LFLD event. Fig. 12(a) shows the results for Stage HF-1. The detected LFLD events (marked by dots) started at approximately 35 m away from the starting point of HF-1 and then gradually spread outwards with time to approximately 115 m away from the injection well. Assuming that the locations are normally distributed, the confidence ellipse for each time segment can be derived using

$$\left(\frac{x}{\sigma_x}\right)^2 + \left(\frac{y}{\sigma_y}\right)^2 = \chi^2 \tag{11}$$

where (x, y) are the East and North coordinates of the confidence ellipse, σ_x and σ_y are the standard deviations at East and North directions, and χ^2 is the value of the χ^2-distribution (for 95% confidence interval, $\chi^2 = 5.991$). The 95% spatiotemporal confidence ellipses for LFLD events are shown with a darker color for an earlier time and a lighter color for a later time as depicted in Fig. 12(a), which clearly indicates that the fracture flow and created fractures expand outward from the injection well. We observe the same phenomena for Stage HF-2 as depicted in Fig. 12(a) (bottom). During the time period 05:25:21–05:54:59 (hour: minute: second) on November 18, 2015, the outer ellipse of the LFLD events crosses through the seismically active zone of Stage HF-1. The fluid injection in HF-1 was performed two days earlier than that in HF-2, therefore, the connectivity between these two adjacent fracture stimulation stages is possible. When proppant is injected during Stage HF-2, the fluid can flow to those preexisting fractures and create new fractures. By contrast, the spatiotemporal distribution of non-LFLD events [see Fig. 12(b)] is mostly randomly (top) or repeatedly (bottom) distributed and does not expand from the injection wells outward with time evolution.

V. Conclusion

To cluster hydraulic fracturing-induced microseismic events recorded in boreholes, we reduce the dimensionality of the event spectrograms using the U-Net deep neural network and then classify the events into ten clusters using GMM. We find four types of microseismic events: 1) the FDLD events; 2) the LFLD event; 3) the HFSD event; and 4) the LFSD event. We compare the proppant injection history with the occurrence times of the LFLD events, FDLD event, and non-LD events, and find that only LFLD events occur during the proppant injection period, while the other types of microseismicity occur before, during, and after proppant injection. We also observe that the cumulative seismic moment of the LFLD events is linearly related to the cumulative proppant injection volume. The spatiotemporal distributions of the LFLD events validate that they are induced by sequential fracture flow, whereas the other types of microseismic events may not be directly related to fracture flow. Our findings strongly suggest that the LFLD events may be induced by the fracture flows during hydraulic fracturing. Therefore, by clustering LFLD events, we can optimize the proppant injection parameters (e.g., time, volume) to improve the efficiency of hydraulic fracturing.

Acknowledgment

This work was completed as part of the Science-informed Machine Learning for Accelerating Real-time Decisions in Oil and Gas (SMART-OG) Initiative (edx.netl.doe.gov/smart). Support for this initiative was provided by the U.S. Department of Energy's (DOE) Office of Fossil Energy and Carbon Management through the National Energy Technology Laboratory (NETL). The authors wish to thank Joseph Renk III (NETL), Grant Bromhal (NETL), Mark McKoy (NETL), Darin Damiani (DOE Office of Fossil Energy and Carbon Management), and Mark Ackiewicz (DOE Office of Fossil Energy and Carbon Management), for programmatic guidance, direction, and support.

Code Availability

The authors modified the existing deep clustering code to align with the goals of their project. The original code can be accessed from https://github.com/NeptuneProjects/RISWorkflow.

References

[1] Z. E. Ross and E. S. Cochran, "Evidence for latent crustal fluid injection transients in Southern California from long-duration earthquake swarms," *Geophys. Res. Lett.*, vol. 48, no. 12, Jun. 2021, Art. no. e2021GL092465.

[2] M. Zecevic, G. Daniel, and D. Jurick, "On the nature of long-period long-duration seismic events detected during hydraulic fracturing," *Geophysics*, vol. 81, no. 3, pp. 113–121, May 2016.

[3] K. Aki and R. Koyanagi, "Deep volcanic tremor and magma ascent mechanism under Kilauea, Hawaii," *J. Geophys. Res., Solid Earth*, vol. 86, no. 8, pp. 7095–7109, Aug. 1981.

[4] M. Fehler, "Observations of volcanic tremor at Mount St. Helens Volcano," *J. Geophys. Res., Solid Earth*, vol. 88, no. 4, pp. 3476–3484, Apr. 1983.

[5] A. Hofstetter and S. Malone, "Observations of volcanic tremor at Mount St. Helens in April and May 1980," *Bull. Seismolog. Soc. Amer.*, vol. 76, no. 4, pp. 923–938, 1980.

[6] G. Rogers and H. Dragert, "Episodic tremor and slip on the cascadia subduction zone: The chatter of silent slip," *Science*, vol. 300, no. 5627, pp. 1942–1943, Jun. 2003.

[7] A. G. Wech, "Cataloging tectonic tremor energy radiation in the cascadia subduction zone," *J. Geophys. Res., Solid Earth*, vol. 126, no. 10, Oct. 2021, Art. no. e2021JB022523.

[8] I. Das and M. D. Zoback, "Long-period, long-duration seismic events during hydraulic stimulation of shale and tight-gas reservoirs—Part 1: Waveform characteristics," *Geophysics*, vol. 78, no. 6, pp. 97–108, Nov. 2013.

[9] B. A. Chouet, "Long-period volcano seismicity: Its source and use in eruption forecasting," *Nature*, vol. 380, no. 6572, pp. 309–316, Mar. 1996.

[10] J. Woods et al., "Long-period seismicity reveals magma pathways above a laterally propagating dyke during the 2014–15 Bárðarbunga rifting event, Iceland," *Earth Planet. Sci. Lett.*, vol. 490, pp. 216–229, May 2018.

[11] H. Hu, A. Li, and R. Zavala-Torres, "Long-period long-duration seismic events during hydraulic fracturing: Implications for tensile fracture development," *Geophys. Res. Lett.*, vol. 44, no. 10, pp. 4814–4819, May 2017.

[12] A. Kumar, E. Zorn, R. Hammack, and W. Harbert, "Long-period, long-duration seismicity observed during hydraulic fracturing of the Marcellus Shale in Greene County, Pennsylvania," *Lead. Edge*, vol. 36, no. 7, pp. 580–587, Jul. 2017.

[13] M. D. Zoback, A. Kohli, I. Das, and M. McClure, "The importance of slow slip on faults during hydraulic fracturing stimulation of shale gas reservoirs," in *Proc. SPE Americas Unconventional Resour. Conf.*, 2012, p. SPE-155476.

[14] D. Bame and M. Fehler, "Observations of long period earthquakes accompanying hydraulic fracturing," *Geophys. Res. Lett.*, vol. 13, no. 2, pp. 149–152, Feb. 1986.

[15] V. Ferrazzini, B. Chouet, M. Fehler, and K. Aki, "Quantitative analysis of long-period events recorded during hydrofracture experiments at Fenton Hill, New Mexico," *J. Geophys. Res., Solid Earth*, vol. 95, no. 13, pp. 21871–21884, Dec. 1990.

[16] R. Wang, Y. J. Gu, R. Schultz, M. Zhang, and A. Kim, "Source characteristics and geological implications of the January 2016 induced earthquake swarm near Crooked Lake, Alberta," *Geophys. J. Int.*, vol. 210, no. 2, pp. 979–988, Aug. 2017.

[17] R. Wang, Y. J. Gu, R. Schultz, A. Kim, and G. Atkinson, "Source analysis of a potential hydraulic-fracturing-induced earthquake near Fox Creek, Alberta," *Geophys. Res. Lett.*, vol. 43, no. 2, pp. 564–573, Jan. 2016.

[18] J. Yang and H. Zhu, "Locating and monitoring microseismicity, hydraulic fracture and earthquake rupture using elastic time-reversal imaging," *Geophys. J. Int.*, vol. 216, no. 1, pp. 726–744, Jan. 2019.

[19] C. Cauzzi et al., "Earthquake early warning and operational earthquake forecasting as real-time hazard information to mitigate seismic risk at nuclear facilities," *Bull. Earthq. Eng.*, vol. 14, no. 9, pp. 2495–2512, Sep. 2016.

[20] L. Linville, K. Pankow, and T. Draelos, "Deep learning models augment analyst decisions for event discrimination," *Geophys. Res. Lett.*, vol. 46, no. 7, pp. 3643–3651, Apr. 2019.

[21] M. Beyreuther, C. Hammer, J. Wassermann, M. Ohrnberger, and T. Megies, "Constructing a hidden Markov model based earthquake detector: Application to induced seismicity," *Geophys. J. Int.*, vol. 189, no. 1, pp. 602–610, Apr. 2012.

[22] S. M. Mousavi, W. L. Ellsworth, W. Zhu, L. Y. Chuang, and G. C. Beroza, "Earthquake transformer—An attentive deep-learning model for simultaneous earthquake detection and phase picking," *Nature Commun.*, vol. 11, no. 1, pp. 1–12, Aug. 2020.

[23] T. Perol, M. Gharbi, and M. Denolle, "Convolutional neural network for earthquake detection and location," *Sci. Adv.*, vol. 4, no. 2, Feb. 2018, Art. no. e1700578.

[24] C. E. Yoon, O. O'Reilly, K. J. Bergen, and G. C. Beroza, "Earthquake detection through computationally efficient similarity search," *Sci. Adv.*, vol. 1, no. 11, Dec. 2015, Art. no. e1501057.

[25] C. Chai et al., "Using a deep neural network and transfer learning to bridge scales for seismic phase picking," *Geophys. Res. Lett.*, vol. 47, no. 16, Aug. 2020, Art. no. e2020GL088651.

[26] W. Zhu and G. C. Beroza, "PhaseNet: A deep-neural-network-based seismic arrival time picking method," *Geophys. J. Int.*, vol. 216, no. 1, pp. 261–273, Oct. 2018.

[27] W. Zhu, I. W. McBrearty, S. M. Mousavi, W. L. Ellsworth, and G. C. Beroza, "Earthquake phase association using a Bayesian Gaussian mixture model," *J. Geophys. Res., Solid Earth*, vol. 127, no. 5, May 2022, Art. no. e2021JB023249.

[28] I. W. McBrearty, A. A. Delorey, and P. A. Johnson, "Pairwise association of seismic arrivals with convolutional neural networks," *Seismological Res. Lett.*, vol. 90, no. 2, pp. 503–509, Mar. 2019.

[29] C. Song, T. Alkhalifah, and U. B. Waheed, "Solving the frequency-domain acoustic VTI wave equation using physics-informed neural networks," *Geophys. J. Int.*, vol. 225, no. 1, pp. 846–859, Dec. 2020.

[30] W. F. Jenkins, P. Gerstoft, M. J. Bianco, and P. D. Bromirski, "Unsupervised deep clustering of seismic data: Monitoring the Ross Ice Shelf, Antarctica," *J. Geophys. Res., Solid Earth*, vol. 126, no. 9, Sep. 2021, Art. no. e2021JB021716.

[31] S. M. Mousavi, W. Zhu, W. Ellsworth, and G. Beroza, "Unsupervised clustering of seismic signals using deep convolutional autoencoders," *IEEE Geosci. Remote Sens. Lett.*, vol. 16, no. 11, pp. 1693–1697, Nov. 2019.

[32] L. Seydoux, R. Balestriero, P. Poli, M. D. Hoop, M. Campillo, and R. Baraniuk, "Clustering earthquake signals and background noises in continuous seismic data with unsupervised deep learning," *Nature Commun.*, vol. 11, no. 1, pp. 1–12, Aug. 2020.

[33] C.-C. Chien, W. F. Jenkins, P. Gerstoft, M. Zumberge, and R. Mellors, "Automatic classification with an autoencoder of seismic signals on a distributed acoustic sensing cable," *Comput. Geotechnics*, vol. 155, Mar. 2023, Art. no. 105223.

[34] S. M. Mousavi and G. C. Beroza, "Machine learning in earthquake seismology," *Annu. Rev. Earth Planet. Sci.*, vol. 51, no. 1, pp. 105–129, May 2023.

[35] N. A. Stegent and C. Candler, "Downhole microseismic mapping of more than 400 fracturing stages on a multiwell pad at the hydraulic fracturing test site (HFTS): Discussion of operational challenges and analytic results," in *Proc. 6th Unconventional Resour. Technol. Conf.*, Houston, TX, USA, 2018, pp. 3754–3781.

[36] J. Kaiser and R. Schafer, "On the use of the I_0-sinh window for spectrum analysis," *IEEE Trans. Acoust., Speech, Signal Process.*, vol. ASSP-28, no. 1, pp. 105–107, Feb. 1980.

[37] C. C. Aggarwal, A. Hinneburg, and D. A. Keim, "On the surprising behavior of distance metrics in high dimensional space," in *Proc. 8th Int. Conf., Database Theory*, London, U.K. Berlin, Germany: Springer, 2001, pp. 420–434.

[38] M. Steinbach, L. Ertöz, and V. Kumar, "The challenges of clustering high dimensional data," in *New Directions in Statistical Physics: Econophysics, Bioinformatics, and Pattern Recognition*. Berlin, Germany: Springer, 2004, pp. 273–309.

[39] I. Goodfellow, Y. Bengio, and A. Courville, *Deep Learning*. Cambridge, MA, USA: MIT Press, 2016.

[40] D. P. Kingma and J. Ba, "Adam: A method for stochastic optimization," 2014, *arXiv:1412.6980*.

[41] C. M. Bishop, *Pattern Recognition and Machine Learning*. New York, NY, USA: Springer, 2006.

[42] K. P. Murphy, *Machine Learning: A Probabilistic Perspective*. Cambridge, MA, USA: MIT Press, 2012.

[43] P. J. Rousseeuw, "Silhouettes: A graphical aid to the interpretation and validation of cluster analysis," *J. Comput. Appl. Math.*, vol. 20, pp. 53–65, Nov. 1987.

[44] S. A. Shapiro, O. S. Krüger, C. Dinske, and C. Langenbruch, "Magnitudes of induced earthquakes and geometric scales of fluid-stimulated rock volumes," *Geophysics*, vol. 76, no. 6, pp. 55–63, Nov. 2011.

[45] M. Galis, J. P. Ampuero, P. M. Mai, and F. Cappa, "Induced seismicity provides insight into why earthquake ruptures stop," *Sci. Adv.*, vol. 3, no. 12, Dec. 2017, Art. no. eaap7528.

[46] Y. Zheng, "Transient pressure surge in a fluid-filled fracture," *Bull. Seismolog. Soc. Amer.*, vol. 108, no. 3, pp. 1481–1488, 2018.
[47] H. Kanamori, "The energy release in great earthquakes," *J. Geophys. Res.*, vol. 82, no. 20, pp. 2981–2987, Jul. 1977.
[48] S. Bentz, G. Kwiatek, P. Martínez-Garzón, M. Bohnhoff, and G. Dresen, "Seismic moment evolution during hydraulic stimulations," *Geophys. Res. Lett.*, vol. 47, no. 5, Mar. 2020, Art. no. e2019GL086185.

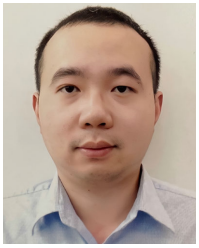

Chenglong Duan received the Ph.D. degree in geophysics from The University of Texas at Dallas, Richardson, TX, USA, in 2022.

He completed his Graduate Research Internship at the Los Alamos National Laboratory (LANL), Los Alamos, NM, USA, in 2021. He has been a Post-Doctoral Fellow at The University of New Mexico, Albuquerque, NM, USA, since 2023. His research interests include full-wavefield imaging methods with applications in micro-earthquake source characterization/Earth structure/volcanology, and machine-learning classification algorithms in seismology.

Lianjie Huang received the B.Sc. degree in physics and the M.Sc. degree in mathematics from Peking University, Beijing, China, in 1985 and 1989, respectively, and the Ph.D. degree in geophysics from the University of Paris 7/Institut de Physique du Globe de Paris, Paris, France, in 1994.

He is a Senior Scientist with the Geophysics Group, Los Alamos National Laboratory (LANL), Los Alamos, NM, USA. His research areas encompass acoustic and elastic-wave modeling, imaging, inversion/tomography, and machine learning with applications to geothermal energy, geologic carbon storage, oil/gas, and cancer detection and characterization.

Michael Gross received the Ph.D. degree from Penn State University, State College, PA, USA, in 1993.

He is currently a Senior Research Scientist at the Los Alamos National Laboratory, Los Alamos, NM, USA. He is also a structural and petroleum geologist with a primary focus on brittle deformation (faults and fractures). He studies the formation and distribution of fractures within the context of mechanical stratigraphy and structural position/tectonic setting. Over the past 20 years, he has been mostly involved in basic research issues; more recently he has been working with industry to apply various techniques of fracture analysis to reservoir characterization and optimization.

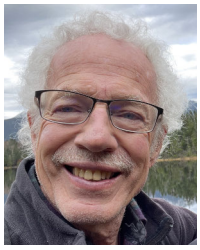

Michael Fehler received the Ph.D. degree from Massachusetts Institute of Technology (MIT), Cambridge, MA, USA, in 1979.

Since then, he has been with the College of Oceanography, Oregon State University, Corvallis, OR, USA, and Los Alamos National Laboratory, Los Alamos, NM, USA, where he was a Leader of the Geophysics Group and later the Division Director of the Earth and Environmental Sciences Division. He is currently a Senior Research Scientist in the Department of Earth, Atmospheric and Planetary Sciences, MIT. He previously served as the Associate Director at Earth Resources Laboratory (ERL), MIT. His research interests include seismic imaging, reservoir characterization, seismic scattering, geothermal energy, and induced seismicity.

Dr. Fehler was the President of the Seismological Society of America from 2005 to 2007. He was the Editor-in-Chief of the *Bulletin of the Seismological Society of America* for nine years.

David Lumley received the B.Sc. and M.Sc. degrees in geophysics and astronomy from The University of British Columbia, Vancouver, BC, Canada, in 1986 and 1989, respectively, and the Ph.D. degree in geophysics from Stanford University, Stanford, CA, USA, in 1995.

He is currently a Professor of Earth sciences and physics at the University of Texas at Dallas (UT Dallas), Richardson, TX, USA, the Cecil and Ida Green Endowed Chair in geophysics, the Department Head of sustainable earth systems sciences, and the Director of the Seismic Imaging and Inversion Laboratory at UT Dallas. Previously, he was a Professor, the Chair in geophysics, and the Founding Director of the Center for Energy Geoscience, The University of Western Australia, Perth, WA, Australia, where he was jointly appointed at the School of Physics and Astrophysics and the School of Earth and Environment. He was the Founder and a Leader of the 4-D Seismic Research Group, Chevron Research, San Ramon, CA, USA, and the Founder and the CEO of Fourth Wave Imaging Corporation (purchased by Fugro in 2007), Aliso Viejo, CA, USA. His research interests include wavefield data recorded with large-N sensor arrays, using man-made sources, and natural sources such as earthquakes and ambient seismic noise. Applications include imaging and time-lapse monitoring of the Earth's subsurface, natural resources, energy, water, fluid flow, CO_2 injection and storage, natural and induced earthquake seismicity, and astrophysical gravitational waves; covering a broad range of scales including the near-surface "critical zone," oceans, sediments, deep aquifers and reservoirs, subduction zones, tectonic crust and mantle, planets and moons, and astrophysics.

Dr. Lumley was a recipient of SEG's J. Clarence Karcher Award.

Stanislav Glubokovskikh received the Ph.D. degree in geophysics (major in physics and mathematics) from Lomonosov Moscow State University, Moscow, Russia, in 2011.

He joined the Berkeley Laboratory in November 2020 to work on seismic characterization and monitoring for diverse purposes: from unconventional reservoirs to geological carbon storage. He is currently a Research Earth Scientist at the Energy Geosciences Division, Lawrence Berkeley National Laboratory, Berkeley, CA, USA. Prior to the Berkeley Laboratory, he was working as a Senior Research Fellow at Curtin University, Perth, WA, Australia, and a number of research institutions in Russia. He is a passionate geoscientist with 12 years experience of in geophysical research and teaching undergraduate and postgraduate courses to geophysicists.